Journal of Biomedical Optics

BiomedicalOptics.SPIEDigitalLibrary.org

Intrauterine photoacoustic and ultrasound imaging probe

Christopher Miranda
Joel Barkley
Barbara S. Smith

SPIE.

Christopher Miranda, Joel Barkley, Barbara S. Smith, "Intrauterine photoacoustic and ultrasound imaging probe," *J. Biomed. Opt.* **23**(4), 046008 (2018), doi: 10.1117/1.JBO.23.4.046008.

Intrauterine photoacoustic and ultrasound imaging probe

Christopher Miranda,[a] Joel Barkley,[b] and Barbara S. Smith[a,*]
[a]Arizona State University, School of Biological and Health Systems Engineering, Smith Research Group, Tempe, Arizona, United States
[b]Maricopa Integrated Health Systems, Department of Obstetrics and Gynecology, Phoenix, Arizona, United States

Abstract. Intrauterine photoacoustic and ultrasound imaging are probe-based imaging modalities with translational potential for use in detecting endometrial diseases. This deep-tissue imaging probe design allows for the retrofitting of commercially available endometrial sampling curettes. The imaging probe presented here has a 2.92-mm diameter and approximate length of 26 cm, which allows for entry into the human endometrial cavity, making it possible to use photoacoustic imaging and high-resolution ultrasound to characterize the uterus. We demonstrate the imaging probes' ability to provide structural information of an excised pig uterus using ultrasound imaging and detect photoacoustic signals at a radial depth of 1 cm. [DOI: 10.1117/1.JBO.23.4.046008]

Keywords: photoacoustic endoscopy; endometrial cancer; ultrasound imaging; deep-tissue imaging; probe.

Paper 170830R received Dec. 28, 2017; accepted for publication Apr. 5, 2018; published online Apr. 26, 2018.

1 Introduction

Endometrial cancer is an abnormal growth of cells in and around the lining (endometrium) of the uterus. It is the single most common cancer of the female reproductive system, with an estimated 700,000 women living with this disease.[1] At some point in their life, 1 in 36 women will be affected.[2] Despite the considerable need, however, there is no single medical test capable of diagnosing endometrial cancer at the point-of-care. The most common symptom of this disease is abnormal uterine bleeding (AUB).[3–5] It has been shown that ∼20% of gynecological visits are due to AUB and additional menstrual irregularities.[6] Due to the high prevalence of endometrial cancer, a patient presenting with AUB and common risk factors, such as obesity, diabetes, or age, must undergo testing to rule out the disease.[5] Of the most common imaging modalities associated with endometrial cancer (i.e., ultrasonography,[7] hysteroscopy,[8] MRI,[9] and PET/CT[10]), transvaginal ultrasonography (TVU) is preferred for visualizing this disease. This is largely due to restrictions, such as cost, time, and access, often associated with the aforementioned imaging modalities.[5,11] TVU is utilized to determine the thickness of the endometrium, which provides some diagnostic information. Endometrial thickness that is below a widely accepted threshold can reliably be used to rule out endometrial cancer in postmenopausal women. However, TVU does not have the sensitivity required to diagnose this disease or exclude it in women prior to menopause.[11–16] To obtain an accurate diagnosis through point-of-care imaging modalities, it may be necessary for the technology to measure angiogenesis in the form of increased microvessel density,[17,18] microvessel count,[19] and intratumoral blood flow.[17,20,21] Doppler ultrasound has had moderate success in this regard but still lacks the sensitivity required to reliably diagnose endometrial cancer.[22–24] Among the available imaging modalities, an unexplored imaging tool that holds the potential to accurately image microvasculature, while retaining the ability to measure endometrial thickness, is photoacoustic imaging (PAI). As such, PAI has recently emerged as a powerful modality for imaging cancer[25–30] and providing insight into diagnostically relevant factors, such as angiogenesis,[31,32] oxygenation,[33–35] microvessel density,[36,37] and blood flow.[38]

The photoacoustic effect is the underlying principle of PAI. In brief, this effect leads to the production of pressure waves caused by sudden thermal expansion, as a result of light absorption. Directing a pulsed laser into tissue and detecting the intensity and time delay of the resulting pressure waves from different spatial locations allows for images to be reconstructed. Although PAI can achieve imaging depths beyond the optical diffusion limit,[39] it is still restricted by the penetration depth of light. Thus, requiring that PAI systems be in close proximity to the objects being imaged. In the case of endometrial cancer, the tissue of interest is located near the center of the body in the transverse plane. This makes it infeasible to apply PAI to the endometrium from outside the body, requiring a system that can achieve close proximity to the inner wall of the uterus. Photoacoustic endoscopy (PAE) has recently emerged as an imaging tool useful for *in vivo* characterization within animal models. Previous applications have included imaging of the vasculature along the esophagus and intestines,[40–43] as well as the plaque in large arteries.[44–48] Due to the small diameter of PAE imaging probes, they are of appropriate size to enter the uterus and gain close proximity to the uterine lining. In most photoacoustic and ultrasound endoscopy imaging probes, however, the imaging depth is constrained to a few millimeters.[41,49–51] The width of the uterine cavity itself is on the order of centimeters,[52] requiring a much deeper imaging depth than is currently reported by PAE systems.

In this paper, we investigate intrauterine photoacoustic (IUPA) imaging and intrauterine ultrasound (IUUS) imaging

*Address all correspondence to: Barbara S. Smith, E-mail: barbarasmith@asu.edu

as potential tools for detecting endometrial cancer and other uterine diseases *in vivo*. For application within the human uterus, at the point-of-care, a dual-IUPA/IUUS imaging probe is housed within an endometrial suction curette (catheter-like device with a diameter of <3 mm). This device is commonly used to extract tissue biopsies from the lining of the uterus. Endometrial biopsies are the current gold standard for diagnostic evaluations of endometrial cancer.[11] To perform the endometrial biopsy procedure, the tissue sampling device is introduced into the uterus and advanced toward the fundus. The curette is then rotated and pulled back along the entire length of the uterus while using suction to collect cell samples of the uterine lining. Due to the function of this device, the shape and design of most commercially available sampling curettes have structural and material properties that allow for the flexibility required to enter the uterus and the torque transmission required for *in utero* rotation. Furthermore, the material properties of these suction curettes are designed for safe contact with the uterine lining and maintain low frictional coefficients with uterine tissue. The dual-modal IUPA/IUUS imaging probe implements a unique transducer frequency, allowing for deep-tissue imaging of over a centimeter in depth. Utilizing 360-deg real-time reconstruction, we are able to capture photoacoustic and ultrasound data within excised pig uteri. This work shows intraorgan use and complete imaging of the uterine lining from the center of the uterine cavity. Imaging the human endometrium with IUPA may open the door for point-of-care detection of endometrial cancer and provide valuable insights into a myriad of uterine diseases. To the best of our knowledge, this is the first reported dual-IUPA/IUUS deep-tissue imaging probe.

2 Materials and Methods

2.1 *System Architecture*

The dual-IUPA/IUUS imaging system is depicted as a schematic in Fig. 1. The light source for the system is a tunable LS-2134-LT40 Nd:YAG/Ti:sapphire Nanosecond Pulsed Laser (Symphotic TII Corporation). The laser provides an excitation light with a full width half maximum (FWHM) of 12 to 15 ns at a pulse repetition rate of 10 Hz with specific wavelength operation at 532 and 1064 nm and tunable wavelength from 690 to 1000 nm. Photoacoustic signals generated by the laser are detected by an unfocused ultrasound transducer, with a center frequency of 15 MHz and a −6-dB fractional bandwidth of 40% (Imasonic Inc.). Signals detected by the transducer are sent to the ultrasound pulser/receiver (5077PR Square Wave pulser/receiver, Olympus Inc.), used to both generate and receive ultrasound signals. Amplification is performed through a 59-dB gain and filtered with a 1- to 10-MHz bandpass filter. A multipurpose reconfigurable oscilloscope (NI PXIe-5170R, National Instruments Corporation) is used for data acquisition and equipped with a built-in field programmable gate array (FPGA). Data are processed and transferred to a computer, where the reconstructed image is displayed in real time. Multipurpose programmable function input/output lines, built in to the FPGA, are used for custom triggering and synchronization of the imaging system.

2.2 *Imaging Probe*

The imaging probe, as displayed in Figs. 1 and 2, is composed of a clear plastic housing made from a commercially available endometrial curette (GynoSampler), with an approximate length of 26 cm and an outer diameter of 2.92 mm. Endometrial curettes are hollow, commercially available devices, with an opening (2 mm) adjacent to the tip used clinically by physicians for sample collection. Down the axis of the curette are two components: (i) transducer and (ii) optical fiber. The ultrasound transducer was custom-designed to fit the opening with an outer diameter of 2 mm and a height of 2.2 mm. The normal of the emitting face of the transducer is positioned perpendicularly to the axis of the probe. The transducer is used as both an ultrasound emitter and receiver. Along the axis of the curette runs both the transducer wire and the optical fiber. Attached to the emitting end of the optical fiber, adjacent to the face of the transducer, is an aluminum-coated 700-μm right-angle prism (4531-0021, Tower Optical Inc.). A UV curing optical adhesive (NOA61, Thorlabs) is used to couple the prism to the tip of the optical fiber. Internal components, including the transducer and optical fiber, are fixed in place with a UV curing adhesive. Polyvinylidene chloride is used to securely wrap the imaging probe. A hollow shaft motor (HH17-101, Applied Motion Products, Inc.) dictates the rotational position of the imaging probe, and a linear stage (ET-200-11, Newmark Systems Inc.) controls the axial position.

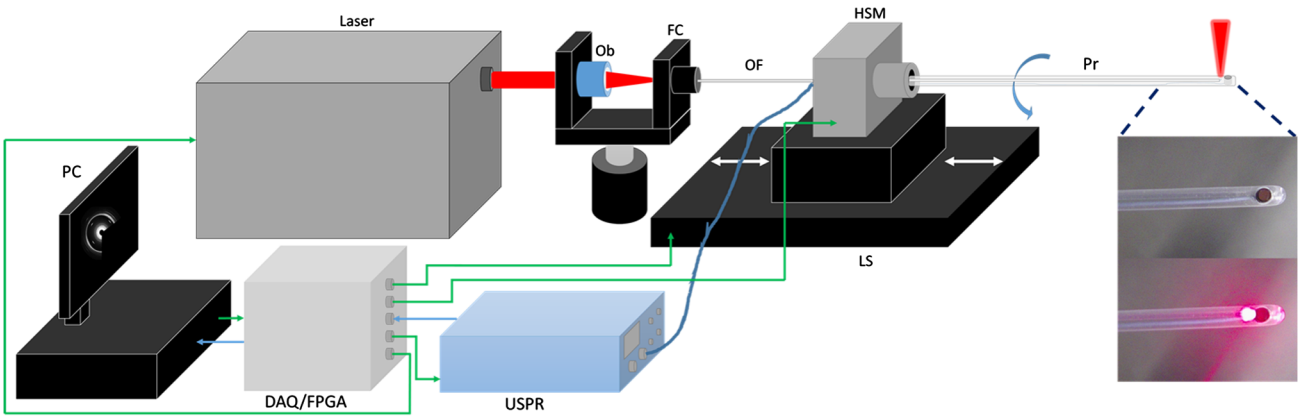

Fig. 1 Schematic showing the system architecture of the IUPA/IUUS endoscopy system. Ob, objective lens; FC, fiber coupler; OF, optical fiber; HSM, hollow shaft motor; USPR, ultrasound pulser receiver; Pr, probe; and DAQ/FPGA, data acquisition/field programmable gate array.

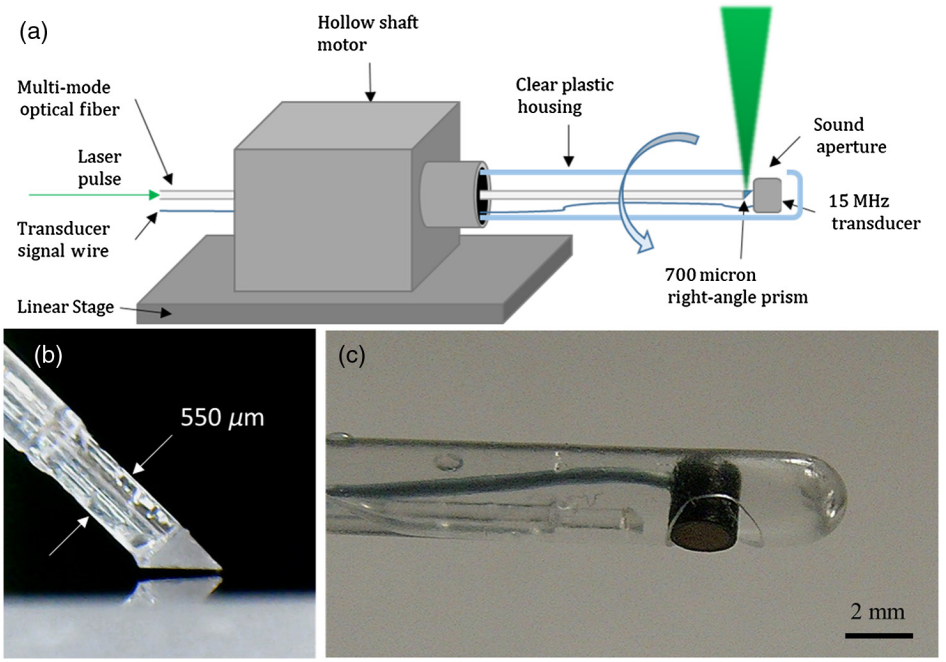

Fig. 2 (a) Schematic of the dual photoacoustic and ultrasound imaging probe system, (b) photo of fiber optic adhered to right-angle prism, and (c) photo of ultrasound transducer and fiber optic adhered to right-angle prism inside the imaging probe.

2.3 *Phantom Tissue Preparation*

The chemical and physical properties of polyvinyl chloride plastisol (PVCP, M-F Manufacturing) were controlled to mimic the acoustic properties of human endometrial tissue. Phantom tissues were fabricated according to methods demonstrated previously.[53] In brief, 100 mL of PVCP was placed in a round bottom flask and heated in an oil bath at 200°C. The mixture was allowed to heat for ∼17 min while stirring under vacuum. PVCP was transferred to a glass cylinder mold with a protruding center to produce a hollow phantom. Parallel to the protruding center, a series of carbon fiber rods with a 250-μm diameter were immediately inserted into the phantom ∼1 cm from the center of the mold. The PVCP remained in the mold until it reached room temperature and solidified. A 21-gauge syringe was used to inject air at two locations and human blood at three locations interspersed between and parallel to the carbon fiber rods. This formed a cylindrical phantom tissue with an outer diameter of 4.5 cm and an inner diameter of 1.3 cm, as shown in Fig. 4(a).

2.4 *Animal Model*

Ex vivo IUPA/IUUS imaging studies were performed on excised adult female pig uteri, acquired within 1-h postslaughter. The section of the uterus, between the uterine horns and the cervix, was removed for use. Immediately upon acquisition, the pig uterus was placed on ice for ∼2 h, to allow for transportation and tissue preparation for imaging. All imaging was completed within 12-h postslaughter. Tissue imaging was performed on a vertically suspended uterus filled with deionized water. Uterus positioning maintained the cervix end on top and the uterine horn end at the bottom. In its vertical orientation, the uterine horn end was securely closed with a clamp. Deionized water was poured into the uterus from the top. The imaging probe was positioned vertically above the cervix end and advanced downward, ∼3.5 cm, along the centerline of the uterus. The uterus was then imaged using 360-deg rotation IUPA/IUUS pullback scans, as described in Sec. 2.5. This study and process of organ acquisition were waived by the oversight bodies at Arizona State University: the Institutional Review Board, the Institutional Biosafety Committee and the Institutional Animal Care and Use Committee.

2.5 *Image Processing and Reconstruction*

Image reconstructions are performed using 800 dual-IUPA/IUUS A-lines, acquired over a 360-deg rotation. IUUS signal generation initiates each A-line. Signal acquisition is maintained for 165 μs. IUPA laser triggering occurs at 135 μs into each A-line, resulting in 30 μs of IUPA acquisition time. After completion of each A-line acquisition, the imaging probe is rotated 0.45 deg (i.e., angular step) by a hollow shaft motor. Between each acquisition, the data are amplified, filtered, transformed, partitioned, averaged, and plotted. In brief, amplification and filtering are performed using a 59-dB gain and a physical 1- to 10-MHz bandpass filter, respectively, by the pulser/receiver. Resulting data are sent to a computer where it is further processed by a custom-designed program in LabVIEW software. Each acquisition is again filtered using a 3- to 8-MHz bandpass filter. A Hilbert transform is applied to the data, and the complex magnitude is subsequently calculated and partitioned into separate IUPA/IUUS data sets. Each individual data set is compressed to a total of 500 representative data points, by averaging clusters of numbers together, resulting in representative data sets with fewer data points. Using a look-up table format, each data point is assigned a group of pixels using a weighted average. Pixels are updated in 13.2 ± 8.3 μs after the completion of each acquisition. Total acquisition and plotting time of both IUUS and IUPA occurs within 200 μs, resulting in a theoretical frame rate of 6.25 frames per second. At a laser firing rate of 10 Hz, a full frame is completed in 80 s. After

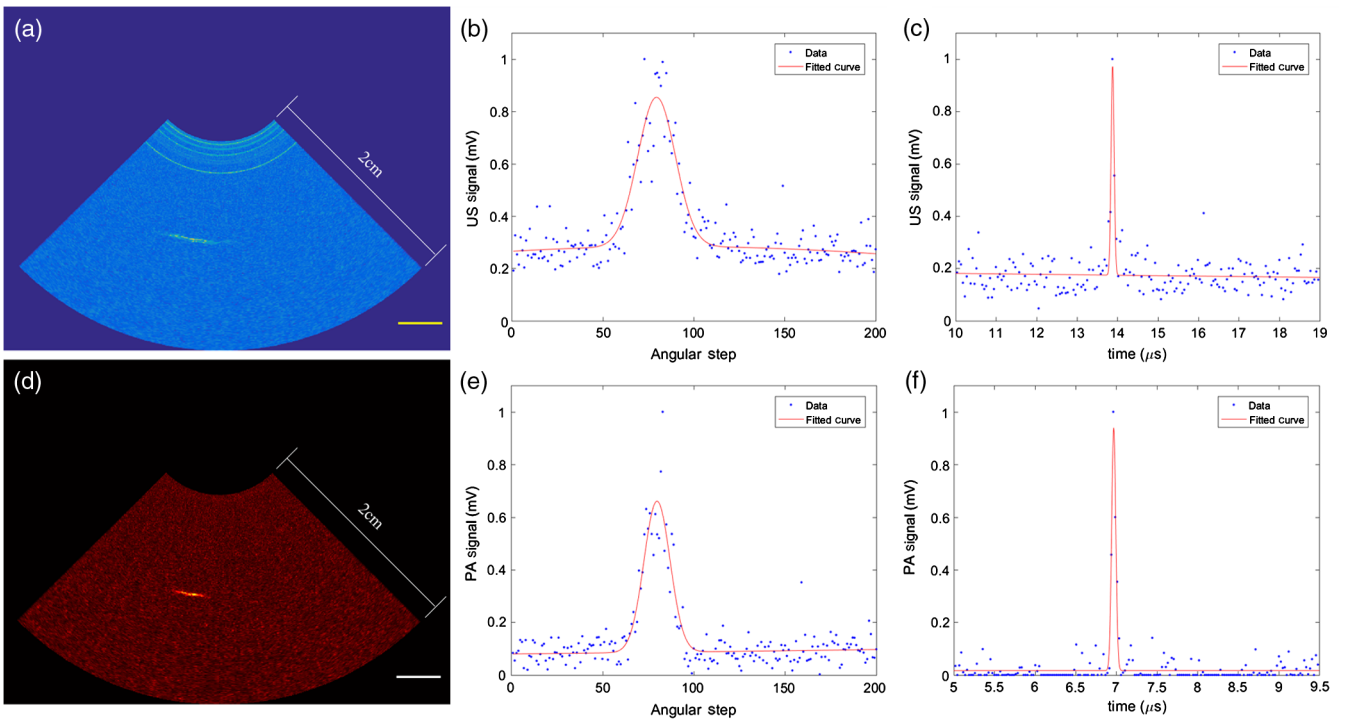

Fig. 3 (a) Ultrasound image reconstruction of 7.2-μm thread at a distance of ~1 cm from imaging probe, (b) transverse resolution measurement of thread in (a), (c) radial resolution measurement of peak signal in (b), (d) photoacoustic image reconstruction of 7.2-μm thread at a distance of ~1 cm from imaging probe, (e) transverse resolution measurement of thread in (d), and (f) radial resolution measurement of peak signal in (e). Scale bars represent 3 mm.

completion of a full 360-deg scan, the axial position of the probe is moved using a linear stage. Imaging continues at the new axial position with the rotation of the probe in the opposite direction of the previous scan.

3 Results

3.1 *Quantifying Imaging Performance Using IUPA and IUUS Probe*

To evaluate the capabilities of the IUPA/IUUS imaging system, a 7.2-μm carbon fiber thread was scanned in the method depicted in Fig. 4(d). The carbon fiber thread was immersed in deionized water and positioned ~1 cm from the imaging probe. Ultrasound and photoacoustic reconstructions of the carbon fiber thread are shown in Figs. 3(a) and 3(d), respectively. Resolution measurements were performed in both the transverse and radial directions. Transverse resolution measurements of the thread correspond to 200 angular steps. At each angular step, the maximum signal was identified, normalized, and plotted for both ultrasound and photoacoustic data sets [Figs. 3(b) and 3(e)]. Results indicate a transverse ultrasound FWHM of 2.0 mm and a photoacoustic FWHM of 1.4 mm. Radial resolution measurements were performed on the angular step that provided the maximum signal, for both ultrasound and photoacoustic acquisitions [Figs. 3(c) and 3(f)]. Measurements of these peaks show an ultrasound FWHM of 239 μm and a photoacoustic FWHM of 143 μm.

Measurements were also performed on 250-μm carbon fiber rods, embedded in a cylindrical phantom with a hollow axis [Fig. 4(a)]. Ultrasound and photoacoustic image reconstructions of the phantom are shown in Figs. 4(b) and 4(c), respectively. Photoacoustic data for these reconstructions were acquired using the method depicted in Fig. 4(d), from within the hollow axis of the phantom. In these experiments, deionized water is used as the acoustic coupling medium. Measurements on the carbon fiber rods were performed in both the transverse and radial directions. To conduct transverse measurements, the maximum ultrasound and photoacoustic signals from a complete 360-deg view are normalized and plotted in Figs. 4(e) and 4(f). From this plot, the ultrasound transverse FWHMs were calculated to be 3.8 and 3.5 mm, at a distance of 1.3 cm for both targets. Radial measurements were conducted at a single angular position corresponding to the maximum ultrasound peaks from the carbon fiber rods. The FWHM for both targets in the radial direction was 629 μm. From Fig. 4(f), photoacoustic FWHMs for the carbon fiber rods were calculated to be 3.2 and 2.8 mm, respectively, at a distance of 1.3 cm for both targets. Radial measurements were conducted at a single angular position corresponding to the maximum photoacoustic peaks from the carbon fiber rods. In the radial direction, the FWHMs were calculated to be 300 and 360 μm, respectively.

3.2 *Ex Vivo Animal Imaging*

Complete 360-deg IUPA/IUUS image reconstructions were performed along a 3.5-cm length of the uterus. A single axial location, ~2 cm down the axis of the uterus, is depicted using IUPA/IUUS imaging in Fig. 5. Human blood and deionized water were injected into two different locations within the muscle of the uterus (myometrium), using an 18-gauge needle. IUPA imaging revealed peak photoacoustic signals [Figs. 5(d) and 5(e)], consistent with the blood injection site. No photoacoustic signals are generated from the water injection site.

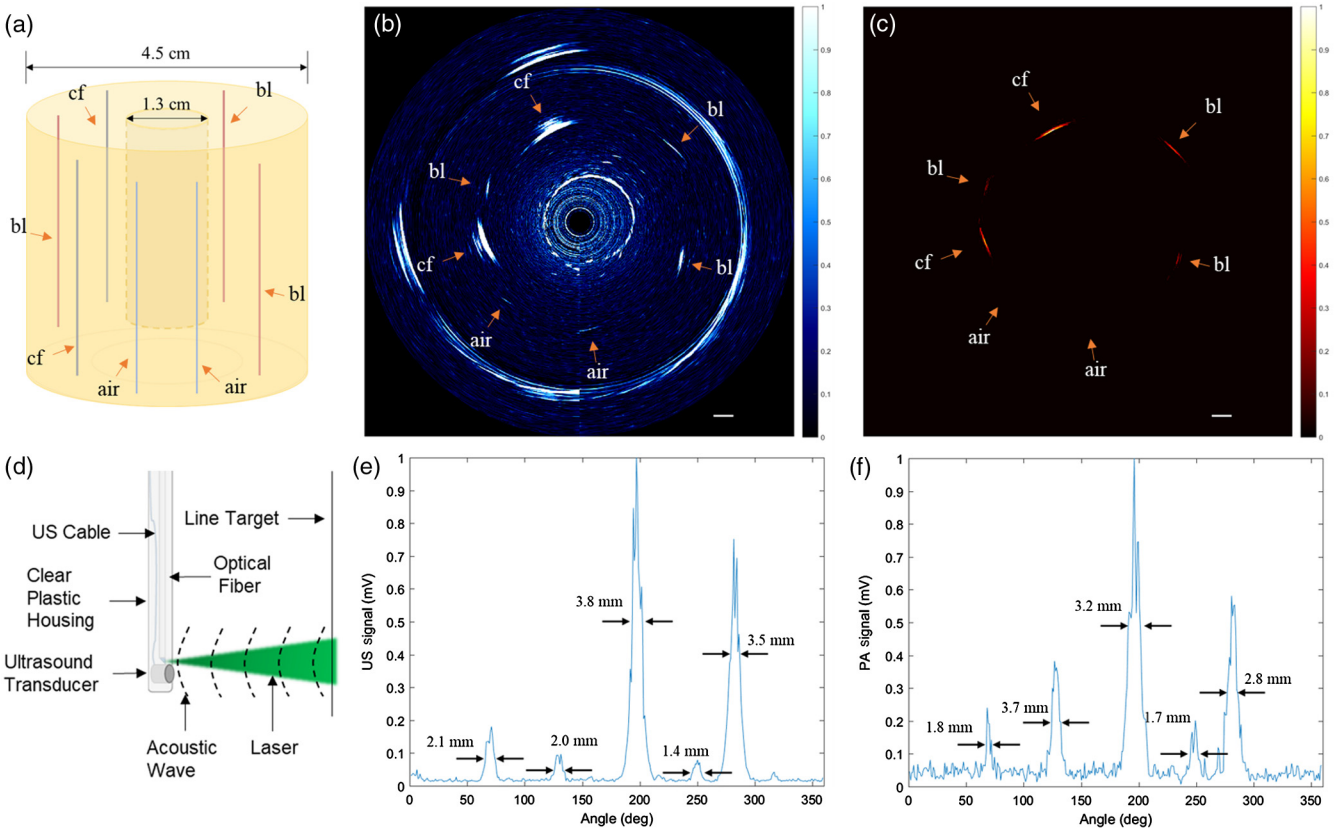

Fig. 4 (a) Hollow cylindrical phantom tissue with two embedded 250-μm carbon fiber rods (cf), three blood injections with 21-gauge needle (bl), and two blank injections (air). (b) and (c) are ultrasound and photoacoustic reconstructions of tissue phantom (a) using method depicted in (d) from the hollow center of the phantom. (e) and (f) are the maximum ultrasound and photoacoustic signals, respectively, received at each angular step. Only data between the inner and outer wall of the phantoms were plotted. Maximum signals normalized to 1. Scale bars in reconstructions represent 3 mm.

Images acquired through real-time reconstructions with the IUPA/IUUS system [Figs. 5(b) and 5(d)] were further improved in MATLAB™ software [Figs. 5(c) and 5(e)]. In the real-time IUUS reconstruction [Fig. 5(b)], the outer wall of the uterus is easily distinguishable, while the inner wall is slightly less distinct. Common contrast enhancement algorithms can be implemented to make the inner wall easier to see. A bright ring shape in the center of the ultrasound reconstructions slightly obscures the inner wall of the uterus. These rings, common to some ultrasound endoscopes,[47,50,51] correspond to the voltage pulse applied to the transducer when it is used as an emitter, and due to their consistency across pulses, can be largely removed from the reconstructions. The real-time IUPA image [Fig. 5(d)] shows bright rings in the center that correspond to the photoacoustic effect induced at the transducer, which is common to some photoacoustic endoscopes.[46,47] Figures 5(c) and 5(e) show IUUS and IUPA reconstructions, respectively, after contrast enhancement and background subtraction is performed. Figure 6 shows IUPA/IUUS reconstructions of a pig uterus with a distinct shape. The distorted shape of Fig. 6(a) is clearly recognizable in both the IUPA/IUUS reconstructions [Figs. 6(b) and 6(c)]. Human blood and deionized water were injected into two different locations within the myometrium, using an 18-gauge needle. As can be seen by the overlapped IUPA/IUUS reconstruction [Fig. 6(d)], the uterus shape and injection site are consistent with Fig. 6(a).

3.3 *Detailed Measurement of the Endometrial Lining within the Pig Uterus*

Measurements were performed to determine the depth of the endometrium in the excised pig uterus. The depths of the infoldings in the endometrium were assumed to be good approximations of the thickness of the endometrium, as opposed to the myometrium. Using a 15- to 20-MHz second-order bandpass filter, instead of the 3- to 8-MHz bandpass filter described in Sec. 2.5, allowed for better visualization of the echoes resembling comet-tail artifacts, as shown in Figs. 7(b) and 7(c). These echoes correspond to the locations of the infoldings as shown in Fig. 7(a). The assumption, here, is that the point at which the echo trails begin is the deepest portion of the infolding. Using the image reconstructions of the high-frequency bandpass filtered data, as shown in Fig. 7, pixel-to-pixel measurements were conducted to calculate the distance between the deepest portion of the infolding and the internal uterine wall. For these measurements, the speed of sound in water (1498 m/s) was used to calculate the depth of the infoldings. Infolding depth was chosen by hand, based on the image reconstructions. Measurements were calculated for the average depth of the infolding (2.0 ± 0.9 mm). For measurements of the overall thickness of the uterine wall, the speed of ultrasound through the human uterus (1616 m/s)[54] was used. Overall thickness was measured (1.0 ± 0.3 cm) by determining the distance

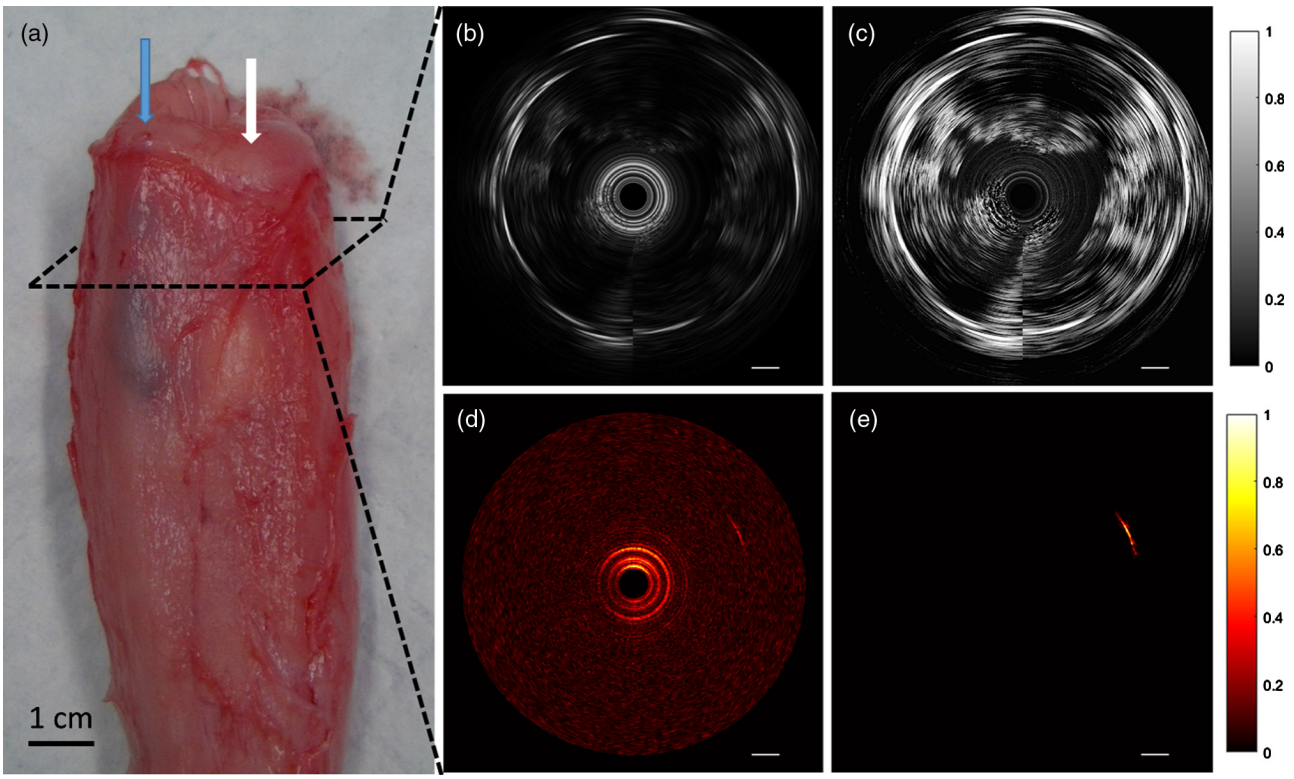

Fig. 5 (a) Photograph of excised adult pig uterus used in the experiments. Blue arrow indicates the location of blood injection. White arrow indicates location of water injection. (b) and (c) Ultrasound reconstruction of pig uterus at the specified cross section. (c) Contrast-enhanced image with background noise removal of (b) post real-time reconstruction. (d) and (e) Photoacoustic reconstruction of corresponding cross section. (e) Contrast-enhanced image with background noise removal of (d) post real-time reconstruction. Scale bars for reconstructed images represent 3 mm.

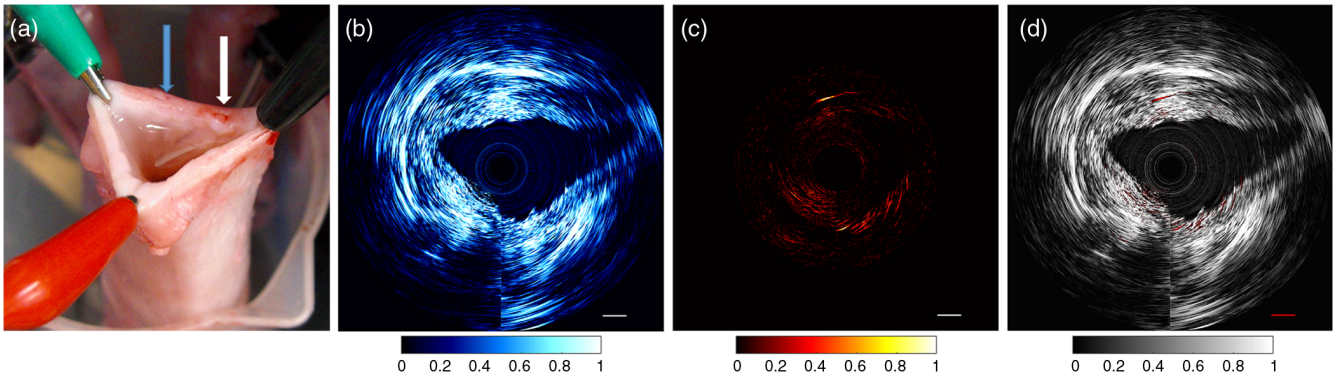

Fig. 6 (a) Photograph of an excised adult pig uterus. Blue arrow indicates the location of blood injection. White arrow indicates location of water injection. (b) Ultrasound reconstruction of pig uterus. (c) Photoacoustic reconstructions of same axial position as (b). (d) Overlap of photoacoustic data on ultrasound data. Scale bar represents 3 mm.

between the inner wall and outer wall by hand based on the image reconstructions.

4 Discussion

Explored here is a deep-tissue IUPA/IUUS imaging probe with potential for imaging endometrial cancer and other uterine diseases. In this paper, we demonstrate several factors for improved clinical applicability, including probe size and imaging depth. The dimensions of the imaging device make it an ideal candidate for *in utero* imaging. An endometrial curette, utilized to collect endometrial biopsies, is used as the housing for this imaging device. Specifically, the proposed imaging procedure is based on that of clinically practiced endometrial biopsies, where a commercially available endometrial suction curette is used to enter the uterus and perform *in utero* rotation. Healthy uterine tissue consists of a few millimeters of endometrium and several centimeters of myometrium. In this work, IUUS imaging depths of up to several centimeters have been achieved through the use of a 15-MHz transducer. This frequency allows for complete

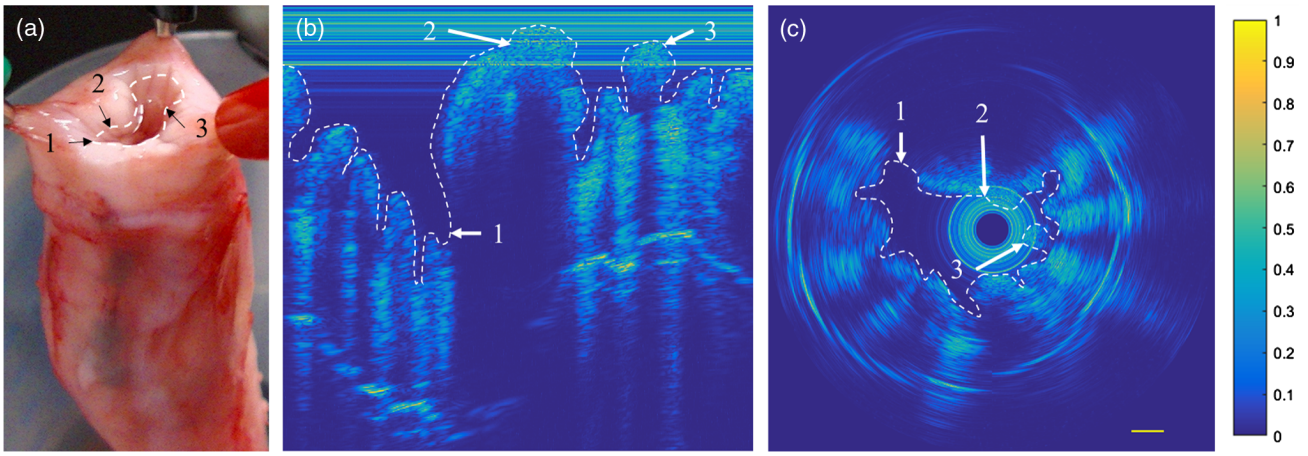

Fig. 7 White-dashed lines manually applied to correspond to the inner wall of the uterus and its infoldings. (a) The experimental setup with suspended pig uterus filled with deionized water for acoustic coupling. (b) Ultrasound image reconstruction of full 360-deg scan in Cartesian coordinates using data filtered to show echoes created by the infolds of the uterine wall. (c) Reconstruction of (b) in polar coordinates. Ultrasound signals were normalized to a value of 1. Numbered points (1), (2), and (3) indicate corresponding locations across images (a), (b), and (c). Scale bar represents 3 mm.

IUUS imaging of the human endometrial cavity and the surrounding uterine tissue. These frequencies make it possible to visualize anatomical abnormalities throughout the endometrium, resulting from diseases such as endometrial cancer. Transducers of different frequencies can be used to optimize tissue imaging at varying depths. The ideal frequency for imaging the entirety of the myometrium in humans will be ∼15 to 25 MHz. Since higher frequency sound waves are attenuated more quickly, frequencies beyond this range may not have adequate imaging depth. In this work, a bandpass filter of 1 to 10 MHz was used on the acquired data, at the expense of some of the useful higher frequency data. This was done to eliminate high-frequency noise generated by the two motors in this system. Based on the combined properties of transducer frequency and excitation light, IUPA is capable of reaching 1 cm in depth for both phantom tissues and pig uteri. Unlike the IUUS imaging depth, which is mainly dependent on frequency, the IUPA imaging depth is dependent on both the frequency of the transducer as well as the properties of the excitation light. For the pig uterus, the frequency range of the detected signals was mainly below 20 MHz. This imaging modality makes it possible to investigate endometrial cancer and other diseases of the endometrium. Opportunity also exists to explore diseases of the myometrium, for the first time using PAI, including submucosal fibroids[55] and sarcomas[56] that manifest close to the endometrium. For this study, an excitation wavelength of 532 nm was used to take advantage of the absorption characteristics of hemoglobin. From a translational standpoint, 532-nm lasers have clinical applicability due to their relatively small size, low cost, and high repetition rate.

The architecture of the uterus requires deep-tissue imaging with high resolution. However, the majority of published PAE imaging systems present resolution measurements below imaging depths of only a few millimeters. To investigate IUPA/IUUS resolution at clinically relevant depths, a 7.2-μm-thick line-target is imaged from a distance of ∼1 cm from the imaging probe [Fig. 3]. At these depths, the ultrasound or excitation laser can be expected to diverge significantly such that the reflected or generated ultrasound signal reaches the transducer surface at some angle relative to the normal of the transducer surface. Ideally, only those ultrasound signals that would arrive at the transducer surface with a zero angle of incidence, with respect to the transducer normal, would be reflected or generated from the target. Results indicate wider FWHMs than reported elsewhere, from targets of similar size, due in part to: (i) greatly increased distance, (ii) the use of an unfocused transducer, and (iii) diverging excitation light. Improvements to the transverse resolution of the imaging system may be possible through the use of a focused ultrasound transducer and/or shaping the excitation light into a collimated or focused beam. Further research is needed to determine the optimal ultrasound focal point, and the beam shape characteristics for light that would maximize the sensitivity and specificity of the imaging probe in detecting uterine diseases. The optimal focal point for the imaging probe is dependent on where the disease would most likely manifest inside the uterus. Distance between the imaging window of the probe and the uterine wall is a function of both its angular and axial position within the uterus.

To accurately model the anatomy of a pig uterus, PVCP phantom tissues were designed in a cylindrical shape with a hollow center. PVCP was chosen as the material for the phantom tissue due to its relatively simple fabrication process and long-term stability. Cancers in the human uterus can often cause anatomical distortions of the uterus.[9] Therefore, clearly identifying the shape of the uterus using dual-IUPA/IUUS imaging may be diagnostically beneficial. To better understand the capabilities of IUPA/IUUS imaging for accurate depictions of uterine abnormalities, the uterus was purposefully distorted, as shown in Fig. 6(a). Alterations to the shape of the inner wall of the uterus are identifiable in both IUPA/IUUS reconstructions. IUPA reconstructions indicate a reduced signal at two of the three corners of the distorted uterus [Fig. 6(c)], ∼1-cm distance from the probe. This is likely due to the inner wall of the uterus moving past the limit of detection of the IUPA probe at these locations. The light exiting the probe with a diverging pattern decreases the ability of the light to successfully generate the photoacoustic effect at the endometrium at larger distances, due to the decrease in fluence.[57] With IUUS imaging, however, the inner wall of the uterus is clearly visible and matches the IUPA reconstructions. IUUS reconstructions clearly depict the outer wall of the uterus.

These results indicate that distortions within the anatomical shape of the uterus can be discerned using IUPA/IUUS imaging, indicating potential for improved diagnostics.

The goal of using IUUS imaging on the pig uterus was to visualize the interface of the endometrium with the myometrium, as is commonly performed with TVU. However, the difference in acoustic impedance between these tissue layers in the pig uterus was not large enough for the interface to be visualized. This could be due to either (i) smaller differences in acoustic impedance in excised pig uteri or (ii) a lack of sensitivity of the imaging probe. Commercially available TVU systems perform at lower transducer frequencies than those utilized in this study. Thus, this imaging probe with a higher transducer frequency should be able to discern smaller differences in acoustic impedance than those of TVU systems. In this work, we utilized higher frequencies but were still unable to differentiate interfaces between the endometrium and the myometrium. Based on physical laws, higher frequencies will discern interfaces of tissues with closer acoustic impedances. Thus, indicating that smaller differences in acoustic impedance are present in excised pig uteri, than *in vivo* human uteri. A notable difference between the pig and human anatomy is the infoldings found along the inner wall of the pig uterus, which are not present in humans. The depth of the infoldings provides insight as to the thickness of the endometrium, since the infoldings do not extend into the myometrium. Measuring the endometrium of the pig uterus serves to prove that the IUPA/IUUS imaging probe will enable accurate *in vivo* imaging. This suggests that the imaging device reported here has potential to improve the diagnostic results of TVU, with respect to endometrial cancer, in human patients at the point-of-care.

5 Conclusion

IUPA/IUUS imaging enables 360-deg real-time reconstruction of the uterine cavity using photoacoustic and ultrasound. In this work, we investigate the potential to diagnose endometrial cancer and other uterine diseases using a miniature dual-mode imaging probe with a unique transducer frequency. Due to the size of the probe, *in utero* imaging is possible. Combined with an imaging depth that exceeds 1 cm, the entire endometrium can be reconstructed from the center of the uterine cavity using IUPA/IUUS. Further investigation of the imaging speed, resolution, and depth will provide insight as to clinical applications for point-of-care diagnosis of uterine diseases.

Disclosures

B.S.S. has a financial interest in Optoacoustics, LLC, which, however, did not support this work.

Acknowledgments

This work was sponsored in part by the National Science Foundation I-Corps Grant No. 1648553. Special thanks to Michael Sobrado for assisting with IUPA/IUUS prototype development.

References

1. N. Howlader et al., "Seer cancer statistics review, 1975–2014," National Cancer Institute (2017).
2. R. L. Siegel, K. D. Miller, and A. Jemal, "Cancer statistics, 2016," *CA—Cancer J. Clin.* **66**(1), 7–30 (2016).
3. J. Kodama et al., "Correlation of presenting symptoms and patient characteristics with endometrial cancer prognosis in Japanese women," *Int. J. Gynecol. Obstet.* **91**(2), 151–156 (2005).
4. J. D. Wright et al., "Contemporary management of endometrial cancer," *Lancet* **379**(9823), 1352–1360 (2012).
5. F. Amant et al., "Endometrial cancer," *Lancet* **366**(9484), 491–505 (2005).
6. W. K. Nicholson et al., "Patterns of ambulatory care use for gynecologic conditions: a national study," *Am. J. Obstet. Gynecol.* **184**(4), 523–530 (2001).
7. S. R. Goldstein, "The role of transvaginal ultrasound or endometrial biopsy in the evaluation of the menopausal endometrium," *Am. J. Obstet. Gynecol.* **201**(1), 5–11 (2009).
8. R. Bedner and I. Rzepka-Gorska, "Hysteroscopy with directed biopsy versus dilatation and curettage for the diagnosis of endometrial hyperplasia and cancer in perimenopausal women," *Eur. J. Gynaecol. Oncol.* **28**(5), 400–402 (2007).
9. K. Tamai et al., "Diffusion-weighted MR imaging of uterine endometrial cancer," *J. Magn. Reson. Imaging* **26**(3), 682–687 (2007).
10. S. L. Antonsen et al., "MRI, PET/CT and ultrasound in the preoperative staging of endometrial cancer—a multicenter prospective comparative study," *Gynecol. Oncol.* **128**(2), 300–308 (2013).
11. W. M. Burke et al., "Endometrial cancer: a review and current management strategies: part II," *Gynecol. Oncol.* **134**(2), 393–402 (2014).
12. P. Morice et al., "Endometrial cancer," *Lancet* **387**(10023), 1094–1108 (2016).
13. R. Smith-Bindman et al., "Endovaginal ultrasound to exclude endometrial cancer and other endometrial abnormalities," *JAMA* **280**(17), 1510–1517 (1998).
14. A. Timmermans et al., "Endometrial thickness measurement for detecting endometrial cancer in women with postmenopausal bleeding: a systematic review and meta-analysis," *Obstet. Gynecol.* **116**(1), 160–167 (2010).
15. I. Symonds, "Ultrasound, hysteroscopy and endometrial biopsy in the investigation of endometrial cancer," *Best Pract. Res. Clin. Obstet. Gynaecol.* **15**(3), 381–391 (2001).
16. J. L. Alcázar and M. Jurado, "Three-dimensional ultrasound for assessing women with gynecological cancer: a systematic review," *Gynecol. Oncol.* **120**(3), 340–346 (2011).
17. C.-N. Lee et al., "Angiogenesis of endometrial carcinomas assessed by measurement of intratumoral blood flow, microvessel density, and vascular endothelial growth factor levels," *Obstet. Gynecol.* **96**(4), 615–621 (2000).
18. H. B. Salvesen, O. E. Iversen, and L. A. Akslen, "Independent prognostic importance of microvessel density in endometrial carcinoma," *Br. J. Cancer* **77**(7), 1140–1144 (1998).
19. D. Ribatti et al., "Neovascularization and mast cells with tryptase activity increase simultaneously with pathologic progression in human endometrial cancer," *Am. J. Obstet. Gynecol.* **193**(6), 1961–1965 (2005).
20. J. L. Alcázar et al., "Intratumoral blood flow analysis in endometrial carcinoma: correlation with tumor characteristics and risk for recurrence," *Gynecol. Oncol.* **84**(2), 258–262 (2002).
21. W.-F. Cheng et al., "Clinical application of intratumoral blood flow study in patients with endometrial carcinoma," *Cancer* **82**(10), 1881–1886 (1998).
22. J. L. Alcazar and R. Galvan, "Three-dimensional power Doppler ultrasound scanning for the prediction of endometrial cancer in women with postmenopausal bleeding and thickened endometrium," *Am. J. Obstet. Gynecol.* **200**(1), 44.e1–44.e6 (2009).
23. M. Emoto et al., "Clinical usefulness of color Doppler ultrasound in patients with endometrial hyperplasia and carcinoma," *Cancer* **94**(3), 700–706 (2002).
24. J. L. Alcazar et al., "Endometrial blood flow mapping using transvaginal power Doppler sonography in women with postmenopausal bleeding and thickened endometrium," *Ultrasound Obstet. Gynecol.* **21**(6), 583–588 (2003).
25. A. P. Jathoul et al., "Deep in vivo photoacoustic imaging of mammalian tissues using a tyrosinase-based genetic reporter," *Nat. Photonics* **9**(4), 239–246 (2015).
26. R. A. Kruger et al., "Dedicated 3D photoacoustic breast imaging," *Med. Phys.* **40**(11), 113301 (2013).

27. M.-L. Li et al., "Simultaneous molecular and hypoxia imaging of brain tumors in vivo using spectroscopic photoacoustic tomography," *Proc. IEEE* **96**(3), 481–489 (2008).
28. A. Aguirre et al., "Potential role of coregistered photoacoustic and ultrasound imaging in ovarian cancer detection and characterization," *Transl. Oncol.* **4**(1), 29–37 (2011).
29. S. Mallidi, G. P. Luke, and S. Emelianov, "Photoacoustic imaging in cancer detection, diagnosis, and treatment guidance," *Trends Biotechnol.* **29**(5), 213–221 (2011).
30. C. Kim et al., "In vivo molecular photoacoustic tomography of melanomas targeted by bioconjugated gold nanocages," *ACS Nano* **4**(8), 4559–4564 (2010).
31. Y. Lao et al., "Noninvasive photoacoustic imaging of the developing vasculature during early tumor growth," *Phys. Med. Biol.* **53**(15), 4203–4212 (2008).
32. R. Siphanto et al., "Serial noninvasive photoacoustic imaging of neovascularization in tumor angiogenesis," *Opt. Express* **13**(1), 89–95 (2005).
33. X. Wang et al., "Noninvasive imaging of hemoglobin concentration and oxygenation in the rat brain using high-resolution photoacoustic tomography," *J. Biomed. Opt.* **11**(2), 024015 (2006).
34. B. Ning et al., "Simultaneous photoacoustic microscopy of microvascular anatomy, oxygen saturation, and blood flow," *Opt. Lett.* **40**(6), 910–913 (2015).
35. M. Schwarz et al., "Three-dimensional multispectral optoacoustic mesoscopy reveals melanin and blood oxygenation in human skin in vivo," *J. Biophotonics* **9**(1–2), 55–60 (2016).
36. E. Zhang et al., "In vivo high-resolution 3D photoacoustic imaging of superficial vascular anatomy," *Phys. Med. Biol.* **54**(4), 1035–1046 (2009).
37. C. Yeh et al., "Microvascular quantification based on contour-scanning photoacoustic microscopy," *J. Biomed. Opt.* **19**(9), 096011 (2014).
38. J. Yao et al., "Label-free oxygen-metabolic photoacoustic microscopy in vivo," *J. Biomed. Opt.* **16**(7), 076003 (2011).
39. L. V. Wang and S. Hu, "Photoacoustic tomography: in vivo imaging from organelles to organs," *Science* **335**(6075), 1458–1462 (2012).
40. J. M. Yang et al., "Three-dimensional photoacoustic endoscopic imaging of the rabbit esophagus," *PLoS One* **10**(4), e0120269 (2015).
41. J.-M. Yang et al., "Simultaneous functional photoacoustic and ultrasonic endoscopy of internal organs in vivo," *Nat. Med.* **18**(8), 1297–1302 (2012).
42. J.-M. Yang et al., "Volumetric photoacoustic endoscopy of upper gastrointestinal tract: ultrasonic transducer technology development," *Proc. SPIE* **7899**, 78990D (2011).
43. J.-M. Yang et al., "Photoacoustic endoscopy," *Opt. Lett.* **34**(10), 1591–1593 (2009).
44. A. B. Karpiouk et al., "Feasibility of in vivo intravascular photoacoustic imaging using integrated ultrasound and photoacoustic imaging catheter," *J. Biomed. Opt.* **17**(9), 096008 (2012).
45. B. Wang et al., "Intravascular photoacoustic imaging," *IEEE J. Sel. Top. Quantum Electron.* **16**(3), 588–599 (2010).
46. B. Wang et al., "Intravascular photoacoustic imaging of lipid in atherosclerotic plaques in the presence of luminal blood," *Opt. Lett.* **37**(7), 1244–1246 (2012).
47. P. Wang et al., "High-speed intravascular photoacoustic imaging of lipid-laden atherosclerotic plaque enabled by a 2-khz barium nitrite Raman laser," *Sci. Rep.* **4**, 6889 (2014).
48. E. Z. Zhang and P. C. Beard, "A miniature all-optical photoacoustic imaging probe," *Proc. SPIE* **7899**, 78991F (2011).
49. X. Bai et al., "Intravascular optical-resolution photoacoustic tomography with a 1.1 mm diameter catheter," *PLoS One* **9**(3), e92463 (2014).
50. S. Sethuraman et al., "Intravascular photoacoustic imaging using an IVUS imaging catheter," *IEEE Trans. Ultrason. Ferroelectr. Freq. Control* **54**(5), 978–986 (2007).
51. K. Jansen et al., "Lipid detection in atherosclerotic human coronaries by spectroscopic intravascular photoacoustic imaging," *Opt. Express* **21**(18), 21472–21484 (2013).
52. E. Merz et al., "Sonographic size of uterus and ovaries in pre- and postmenopausal women," *Ultrasound Obstet. Gynecol.* **7**(1), 38–42 (1996).
53. S. E. Bohndiek et al., "Development and application of stable phantoms for the evaluation of photoacoustic imaging instruments," *PLoS One* **8**(9), e75533 (2013).
54. A. Keshavarzi et al., "Attenuation coefficient and sound speed in human myometrium and uterine fibroid tumors," *J. Ultrasound Med.* **20**(5), 473–480 (2001).
55. E. A. Stewart, "Uterine fibroids," *Lancet* **357**(9252), 293–298 (2001).
56. P. B. Clement, "The pathology of uterine smooth muscle tumors and mixed endometrial stromal-smooth muscle tumors: a selective review with emphasis on recent advances," *Int. J. Gynecol. Pathol.* **19**(1), 39–55 (2000).
57. M. Xu and L. V. Wang, "Photoacoustic imaging in biomedicine," *Rev. Sci. Instrum.* **77**(4), 041101 (2006).

Christopher Miranda received his BS and MS degrees in biomedical engineering from Arizona State University. Currently, he is a PhD candidate at the School of Biological and Health Systems Engineering, Arizona State University. His research interests include biomedical imaging, ultrasound and photoacoustic imaging, technology development, image processing, image reconstruction, and probe development.

Joel Barkley received his BS degree in biochemistry from the University of Nebraska in 2005 and his MD degree from Creighton University School of Medicine in 2010. He performed his residency training in obstetrics and gynecology, received accreditation from the American Registry of Diagnostic Medical Sonographers, and a certificate in women's imaging from Maricopa Integrated Health System (MIHS) in 2015. Currently, he is the director of gynecologic ultrasound at MIHS.

Barbara S. Smith received her BS degree in industrial engineering from Michigan State University in 2003 and her PhD in biomedical engineering from Colorado State University in 2012. She performed her postdoctoral research at Harvard University (with George M. Whitesides). She began her independent career as an assistant professor in biological and health systems engineering at Arizona State University in 2015. Her current research interests include translational diagnostics, biomedical imaging, and biomarker detection.